Catalyst Performance Studies on the Guerbet Reaction in a Continuous Flow Reactor Using Mono- and Bi-Metallic Cu-Ni Porous Metal Oxides

Xiao-Ying Xi [1], Zhuo-Hua Sun [2] [iD], Hua-Tang Cao [3] [iD], Yu-Tao Pei [3] [iD], Gert H. ten Brink [4], Peter J. Deuss [1] [iD], Katalin Barta [2,5] and Hero J. Heeres [1,*]

[1]   Green Chemical Reaction Engineering, Engineering and Technology Institute Groningen, University of Groningen, Nijenborgh 4, 9747 AG Groningen, The Netherlands; x.xi@rug.nl (X.-Y.X.); p.j.deuss@rug.nl (P.J.D.)

[2]   Stratingh Institute for Chemistry, University of Groningen, Nijenborgh 4, 9747 AG Groningen, The Netherlands; sunzhuohua@yahoo.com (Z.-H.S.); k.barta@rug.nl (K.B.)

[3]   Department of Advanced Production Engineering, Engineering and Technology Institute Groningen, Faculty of Science and Engineering, University of Groningen, Nijenborgh 4, 9747AG Groningen, The Netherlands; huatang.cao@manchester.ac.uk (H.-T.C.); y.pei@rug.nl (Y.-T.P.)

[4]   Zernike Institute for Advanced Materials, University of Groningen, Nijenborgh 4, 9747 AG Groningen, The Netherlands; g.h.ten.brink@rug.nl

[5]   Department of Chemistry, Organic and Bioorganic Chemistry, University of Graz, Heinrichstrasse 28/II, Graz 8010, Austria

*   Correspondence: h.j.heeres@rug.nl; Tel.: +31-50-36-34174

Abstract: Higher alcohols like 1-butanol are considered important biofuels with superior properties compared to the more readily available bio-ethanol. An attractive route to prepare 1-butanol from ethanol is the Guerbet reaction. We here report the use of hydrotalcite-derived mono- (Cu-PMO or Ni-PMO) and bi-metallic (CuNi-PMO) porous metal oxide catalysts for the Guerbet coupling of ethanol to 1-butanol in a continuous flow reactor (320 °C, 0.1 MPa, LHSV = 15 mL g^{-1} h^{-1}) at extended times on stream (~160 h). Two distinct regimes with different product distributions were observed for the Cu-PMO and CuNi-PMO catalyst with time on stream. At the start of the run, the initial conversion of ethanol dropped from about 85% to less than 20% after 60 h and acetaldehyde was the main product (regime 1). At prolonged times on stream (60–160 h), fairly constant low conversions of ethanol (14%) were observed and 1-butanol was the main product (regime 2). Performance of the monometallic Cu-PMO catalyst in terms of 1-butanol yield and stability was lower compared to the bi-metallic CuNi-PMO. Detailed catalyst characterization studies (XRD, H$_2$-TPR, sorption of acrylic acid, TGA, TEM, HAADF-STEM, and EDS mapping) on both fresh and spent CuNi-PMO taken at various times on stream was performed to determine the changes in catalyst morphology and composition during a run, and particularly to obtain information on changes in catalyst structure operating in regime 1 or 2. The change in chemoselectivity is in line with an increase in basicity of the catalyst at extended runtimes.

**Keywords:** ethanol; 1-butanol; Guerbet reaction; porous metal oxides; catalyst deactivation

1. Introduction

Bio-ethanol produced from renewable biomass using fermentative approaches is an important commercially available biofuel [1,2]. Though widely used, it has some major drawbacks, such as a lower energy density (70%), a higher vapor pressure, and higher water solubility than gasoline [3]. This has

inspired the search for suitable higher alcohol alternatives such as 1-butanol [4]. When compared to ethanol, the latter has an energy density closer to gasoline (90%), lower miscibility with water, and can be blended with gasoline at higher concentrations [5].

Beside well-established technologies for higher alcohol synthesis, including fermentative routes [6] and syngas conversion [7], the Guerbet coupling of ethanol to 1-butanol has emerged as an attractive alternative [8]. The reaction proceeds via multiple steps involving: 1) dehydrogenation of ethanol to form acetaldehyde; 2) aldol condensation of the resulting acetaldehyde; 3) dehydration to form crotonaldehyde; and 4) hydrogenation of the unsaturated condensation products to give 1-butanol (Scheme 1). Besides the desired Guerbet pathway, a number of side reactions may occur, among others the formation of diethyl ether by ethanol etherification, the formation of ethyl acetate by the Tishchenko reaction involving acetaldehyde and subsequent coupling reactions of 1-butanol [9]. To favor the Guerbet coupling to 1-butanol, catalysts need to be employed with a proper balance between acidic and basic sites, and dehydrogenation/hydrogenation activity [10–13]. Advances related to catalyst development and suitable catalyst compositions for the Guerbet reaction have been summarized in several excellent reviews [8,9,14,15]. Well-established catalysts include MgO, MgAlO$_x$, and hydroxyapatites [16–18]. Among them, hydrotalcite-derived MgAlO$_x$ has attracted much attention due to its tunable basicity [19], for instance, by adjusting the Mg/Al ratio [16,20,21]. Transition metals are often added to the hydrotalcite formulation and function as the dehydrogenation/hydrogenation catalyst. The metals are typically introduced during the synthesis of hydrotalcite, allowing for cooperative interactions between the basic sites of the hydrotalcite surface and supported metal species [19].
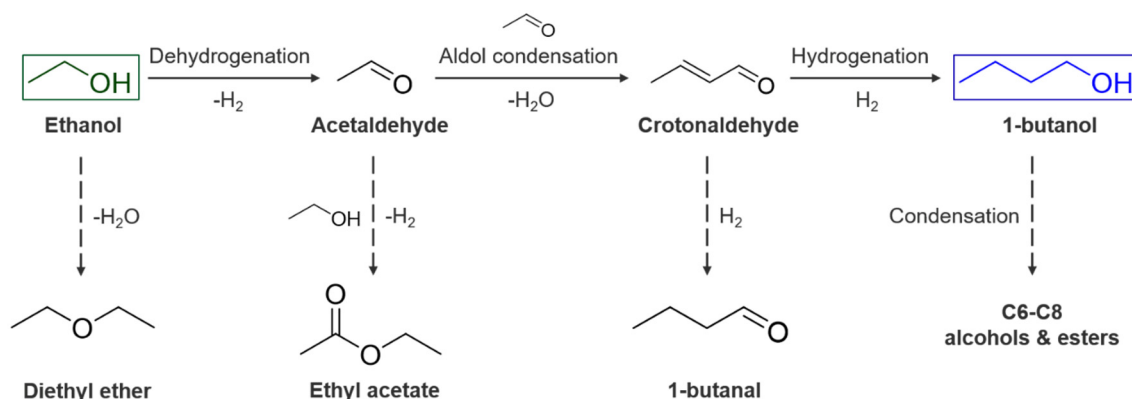
Scheme 1. Reaction network for the Guerbet coupling of ethanol showing the main and side reactions.

Among the possible metals studied, Cu is the most widely used for the Guerbet coupling of alcohols [22]. For instance, Bravo-Suárez et al. reported that the incorporation of Cu in MgAlO$_x$ has a very positive effect on the conversion of methanol and ethanol to C$_{3+}$ alcohols. However, considerable amounts of C$_{3+}$ esters were formed as byproducts [23]. Studies have shown that ester formation is linked to the Cu loading [24]. In detail, a number of Cu-MgAlO$_x$ catalysts with a range of Cu contents (1.0–7.6%) was prepared and tested, and the catalysts with the lowest Cu loading (1.0%) gave the least ester formation [25]. These observations were rationalized by considering that lower amounts of Cu led an increase in the number of basic sites and a reduction in the reducibility of Cu.

Improved catalyst activity and product selectivity to higher alcohols can be achieved by the introduction of metal dopants such as Ni [26]. For instance, a bi-metallic CuNi-MgAlO$_x$ catalyst displayed remarkable higher activity and selectivity to fully hydrogenated β-branched alcohols for the Guerbet reaction of 1-octanol using KOH as a homogeneous base [27]. It was suggested that Ni favors the final hydrogenation step in the reaction network. We have previously reported that hydrotalcite-derived Cu-Ni-doped porous metal oxides (CuNi-PMO) are excellent catalysts for the conversion of ethanol to 1-butanol (22% yield) without the need of a homogeneous base [28].

The addition of Ni suppresses the formation of ethyl acetate, the yield of which was very high over the PMO catalyst containing only Cu.

While essential for further development, Guerbet reaction studies with a focus on continuous operation and catalyst stability are limited. Most studies are exploratory in nature and use batch setups, which do not provide detailed information on catalyst stability. In addition, such batch reactions are not representative for continuous runs as water accumulation occurs to a significant extent [29], which may have a major impact on catalyst structure and thus catalyst performance in terms of activity selectivity as well as stability. Hernández et al. studied the self-condensation of 1-octanol using CuNi-MgAlO$_x$ in a batch reaction system with KOH (1.5 wt%) as a homogeneous base at 225 °C and found that the Cu only catalyst is less stable than the bi-metallic one, among others due to Cu leaching. The higher stability of the bi-metallic catalyst was ascribed to a stabilizing effect of Ni on Cu^{2+} species, leading to a reduced tendency for Cu leaching [27]. Bravo-Suárez et al. reported significant deactivation of the MgAlO$_x$ catalyst in continuously operated vapor-phase methanol and ethanol coupling reactions at 250 °C [23]. Adsorbed oligomeric forms of formaldehyde and acetaldehyde were observed by in situ FTIR, and these species were considered detrimental for activity due to blockage of catalytic sites. DRIFT experiments by Quesada et al. for ethanol condensation in a continuous setup also showed that catalyst deactivation is due to strong adsorption of intermediates and the formation of oxygenated oligomers with more than four carbon atoms [30]. However, systematic studies correlating the changes of catalytic performance with catalyst structure and morphology are scarce. The only example is a study by Silvester et al. using ethanol and carbonate-containing hydroxyapatites as the catalysts in a continuous setup. The evolution of activity with the time on stream was reported though detailed catalyst studies are lacking [31].

Herein, we report on the use of hydrotalcite-derived monometallic Cu and Ni as well as a bi-metallic Cu-Ni PMO catalyst for the Guerbet reaction to convert ethanol to 1-butanol in a continuous flow reactor. The major aim was to use flow chemistry as a first step in scale-up and to assess catalyst stability and possible morphological changes linked to increased time on stream. For this purpose, we have determined ethanol conversion and product distribution for three catalysts at extended runtimes (up to 160 h) to identify the best catalyst in terms of activity, selectivity, and stability. In addition, characterization studies were performed to obtain insights into changes in the catalyst structure and morphology during runtime.

2. Results and Discussion

2.1. Characterization of the Fresh Catalysts

The porous metal oxide (PMO) catalysts were prepared by calcination of the hydrotalcite precursors. The catalyst characterization data including chemical composition (ICP-OES, Table S1), textual properties (Table S1), and XRD patterns (Figure S1) were reported earlier by us with regards to studies in batch setups [28], and as such, only the most relevant data will be given here. The actual composition of the catalysts is very close to the theoretical values (Table S1), indicating that the co-precipitation process for catalyst preparation is effective. The XRD patterns of the three PMO catalysts display a MgO phase with low crystallinity (JCPDS card No. 00-045-0946), similar to the reported XRD pattern of PMO alone [28]. The Al^{3+}, Cu^{2+}, and/or Ni^{2+} cations are likely incorporated in the MgO structure to form a mixed oxide [25,27,32]. Discrete CuO and NiO nanoparticles are neither detectable in the XRD patterns nor in the TEM images (Figure S2), indicating that these are small and highly dispersed.

The H$_2$-TPR profiles for the three PMO catalysts are shown in Figure 1. The Ni-PMO catalyst shows a broad peak centered at 335 °C and a more defined one centered at 770 °C. The first peak is associated with the reduction of NiO on the surface of the Mg-Al mixed oxide. The second is ascribed to the reduction of Ni^{2+} species present in a Ni-Mg-Al solid solution, indicating uniform incorporation of Ni^{2+} when preparing the parent hydrotalcite precursor [27,33,34]. In contrast, Cu-PMO catalyst

only shows one clear reduction peak centered at around 180 °C, which is associated with reduction of CuO species present on the surface of the Mg-Al oxide [35,36]. The formation of these highly reducible CuO species derives from weak interactions of Cu^{2+} with the parent hydrotalcite structure leading to segregation as CuO during the calcination process [27,32,37,38]. The H_2-TPR profiles for the bi-metallic CuNi-PMO catalyst show two reduction peaks. The first peak (200 °C) is associated to the reduction of Cu^{2+} species in the structure [36]. Compared to the monometallic Cu-PMO, it has shifted to higher temperature, possibly due to changes in the Cu geometry induced by the presence of Ni^{2+} [27,39,40]. The second peak (650 °C) related to the reduction of Ni^{2+} species in the Mg-Al mixed oxide structure has shifted to lower temperature in comparison with that of Ni-PMO. This effect has been reported for hydrotalcite-derived catalysts [37,41] and is due to a spillover effect. Both the shift of the Cu^{2+} reduction peak to higher temperature and the Ni^{2+} reduction peak to lower temperature for CuNi-PMO suggest a synergetic interaction between the two cations [42,43].
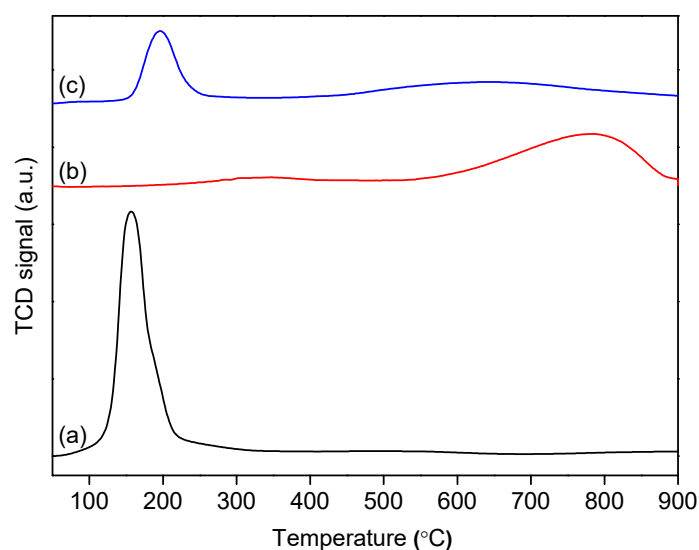

Figure 1. H_2-TPR profiles of fresh Cu-PMO (**a**), Ni-PMO (**b**), and CuNi-PMO (**c**) catalysts.

2.2. Guerbet Coupling of Ethanol in a Continuous Setup

The main objective of the present contribution is to obtain information on catalyst stability for the three selected catalysts. As such, experiments using the three PMO catalysts were carried at an intermediate temperature of 320 °C, a low pressure of 0.1 MPa, and LHSV (liquid hourly space velocity) of 15 mL g^{-1} h^{-1} in a continuous setup.

The ethanol conversion and liquid product distribution versus time on stream for an experiment with the CuNi-PMO catalyst is given in Figure 2. Two distinct regimes are visible, an initial stage where the conversion of ethanol is a strong function of the runtime (0–60 h) and a second one where the ethanol conversion is constant (60–170 h). Furthermore, a remarkable change in the chemoselectivity is observed. In the first stage (0–60 h), the main product is acetaldehyde, together with some ethyl acetate, 1-butanal, and diethyl ether. The carbon balance in regime 1 is far from quantitative (Figure S3), which might be due to loss of volatile compounds (e.g., diethyl ether, acetaldehyde) in the gas-liquid separator or the formation of permanent gases such as methane, CO, and CO_2 [28]. During this first stage, the 1-butanol selectivity increases from 2.8% to 49.9%. In regime 2 (60–168 h), 1-butanol is the main product (~71%), ethyl acetate formation is very limited, and some diethyl ether is detected. Thus, we can conclude that the catalyst structure is changing during time on stream and that only after 60 h, a stable catalyst with a high selectivity for 1-butanol is formed, though at a lower conversion level.
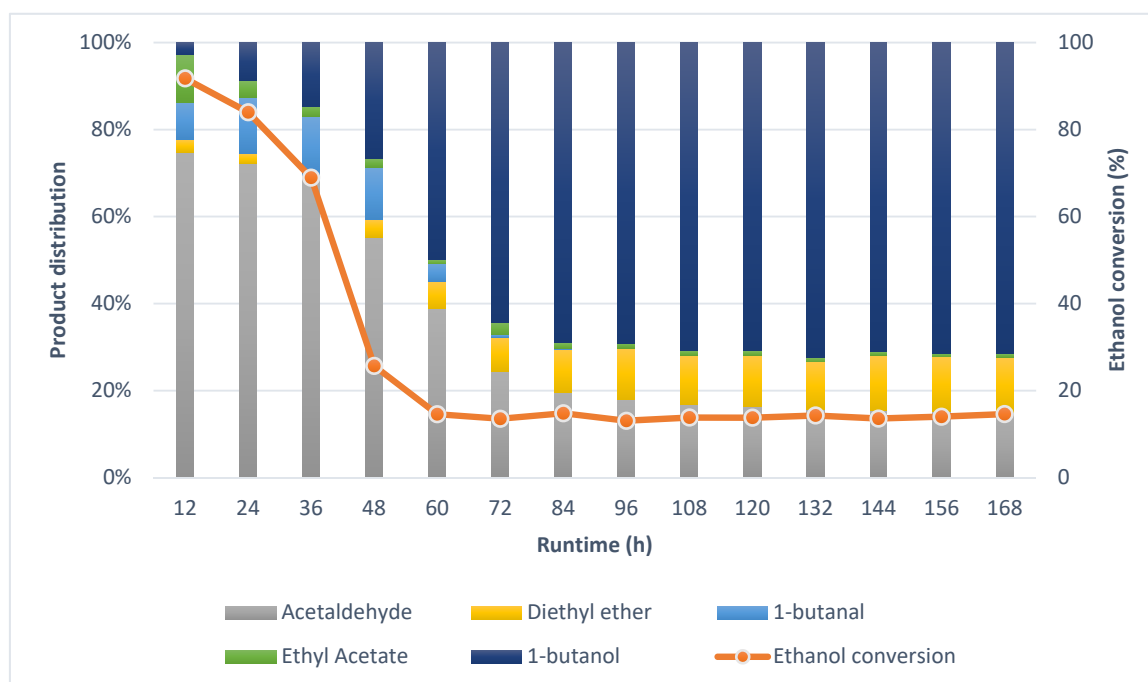
Figure 2. Product distribution and ethanol conversion versus runtime for the CuNi-PMO catalyst. Reaction conditions: 320 °C, 0.1 MPa, LHSV=15 mL g^{-1} h^{-1}.

An experiment using the monometallic Cu-PMO catalyst was performed at similar process conditions and the results are given in Figure 3. The overall trends are similar as found for the bi-metallic Ni-Cu catalyst, viz. a drop in ethanol conversion in the first 60–70 h, followed by a regime with a by far lower ethanol conversion (>72 h). In both regimes, the chemoselectivity is again remarkably different. The obtained yield of 1-butanol first increased from 0.3% (12 h) to 1.6% (72 h), then changed to around 1.9% in regime 2 (Figure S4). However, the 1-butanol selectivity in regime 2 is much lower than for the CuNi-PMO catalyst (40.3% vs. 72.4%), and considerable amounts of acetaldehyde are present (Figure S5). In addition, the ethanol conversion in regime 2 shows a decreasing trend (Figure 3, Figure S6), which suggests that the stability of the Cu-PMO is lower compared to the CuNi-PMO catalyst.
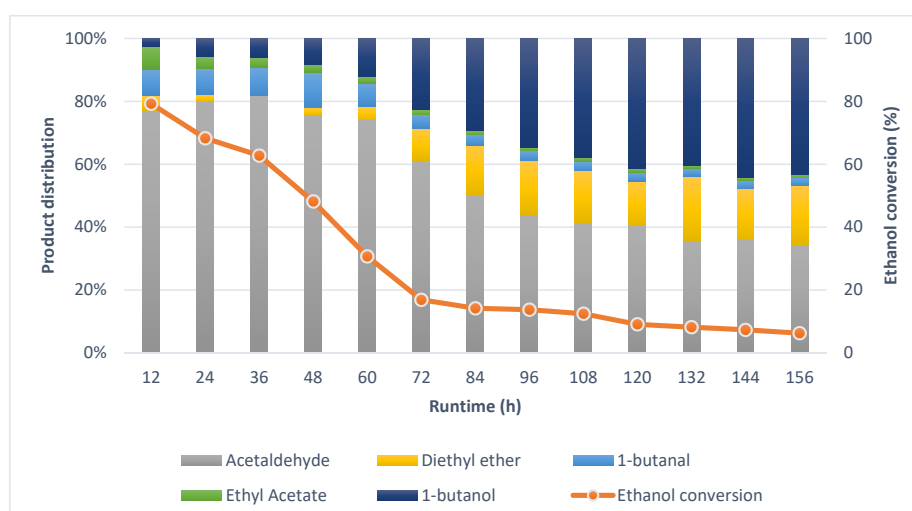

Figure 3. Product distribution and ethanol conversion versus runtime for the Cu-PMO catalyst. Reaction conditions: 320 °C, 0.1 MPa, LHSV = 15 mL g^{-1} h^{-1}.

For comparison, an experiment at similar conditions was performed with the monometallic Ni-PMO catalyst (Figure S7). Catalyst performance was remarkably different and ethanol conversion was about 20% for the complete runtime (156 h). However, 1-butanol was not formed, and only acetaldehyde in low amounts (<1% yield) was detected. As such, and in line with literature data, the presence of Cu in the catalyst formulation is essential to obtain significant amounts of higher alcohols. In addition, promotion of the Cu-PMO catalysts with Ni leads to a considerable improvement in catalyst performance, viz. a higher 1-butanol selectivity and improved catalyst stability in regime 2.

2.3. Characterization of Spent Catalysts

To gain insights in the changes in ethanol conversion and chemoselectivity versus runtime, several experiments were performed at different runtimes using the CuNi-PMO catalyst. After each experiment, the catalysts were characterized using XRD, H_2-TPR, sorption of acrylic acid, TGA, TEM, HAADF-STEM, and EDS to reveal changes in catalyst structure.

The total surface basicity of the various CuNi-PMO samples was determined by the irreversible adsorption of acrylic acid (pK_a = 4.3) [44,45]. Basicity is an important parameter as the basic sites promote the aldol condensation step in the reaction network. The basicity versus the runtime is given in Figure 4 and shows that the basicity initially increases with runtime until about 80 h and then remains about constant. As such, basicity changes may play a role when explaining catalyst performance versus runtime (vide infra). The basicity range (0.2–0.6 mmol g^{-1}) found for the CuNi-PMO catalyst in this work is in good agreement with that of hydrotalcite-derived materials determined by temperature-programmed desorption of CO_2 (0.2–0.8 mmol g^{-1}) [25,46] or sorption of acrylic acid (0.3–0.7 mmol g^{-1}) [47].
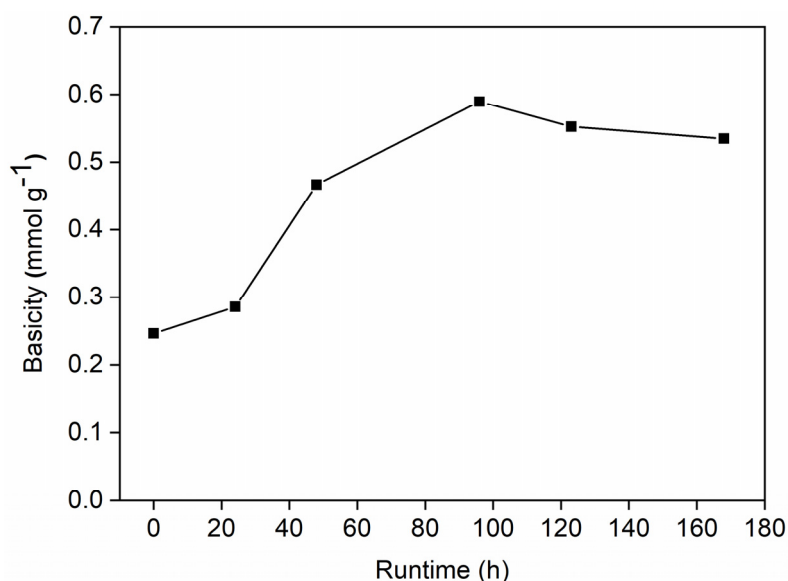

Figure 4. Basicity of the CuNi-PMO catalyst versus runtime.

Representative TEM images for the CuNi-PMO samples at different runtime are given in Figure S8. The fresh CuNi-PMO sample shows only flake-like Mg-Al mixed oxides without any discrete metal nanoparticles. At prolonged runtimes (>48 h), the formation of well-dispersed nanoparticles was observed of which the average diameter increased slightly with runtime (from 3.3 to 5.0 nm, see Figure 5). These nanoparticles likely are either composed of Cu^0 or Cu^0-Ni^0 mixed metal nanoparticles formed by reduction of CuO and NiO by ethanol during the reaction [48–50].
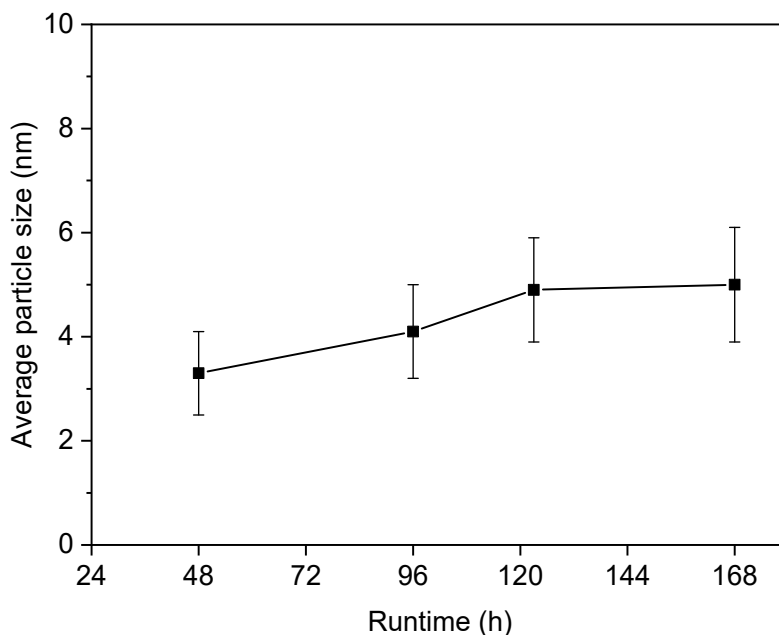
Figure 5. Average nanoparticle size of the CuNi-PMO catalyst obtained at different runtime.

The change in composition of the nanoparticles is also confirmed by H_2-TPR data (Figure S9) of the postreaction samples, which shows an overall broadening of the original distinct CuO (~200 °C) and NiO (~650 °C) signals in the graph of the fresh catalyst. In particular, the signals originating from CuO (~200 °C) are lowered during runtime, while a complex broadened signal around the main reduction peak for NiO (~650 °C) is still observed after 168 h. In line with the H_2-TPR results, FTIR spectra (Figure S10) of the fresh and spent CuNi-PMO (168 h) show that the two peaks (430 and 484 cm^{-1}) attributed to Cu-O disappeared after the reaction. As the reduction temperature of CuO is much lower than that of NiO (Figure 1) and the fact that CuO reduction takes place at much faster rate than NiO [51], the nanoparticles are expected be rich in Cu^0 and contain smaller amounts of Ni^0. The presence of Cu^0 (and not Cu^I) is also confirmed by HRTEM (vide infra).

XRD analyses were performed to gain insights in the composition and size of the nanoparticles in the catalyst samples. Unfortunately, it proved not possible to identify the metallic peaks for Cu^0 or Cu^0-Ni^0 in the XRD spectra (Figure S11) for all the postreaction CuNi-PMO samples because of the presence of small nanoparticle sizes (Figure 5), leading to extensive broadening of the peaks. Alternatively, the nanoparticles might mainly be amorphous, and the reflections of them may overlap with MgO.

A STEM dark-field image combined with EDS mapping of CuNi-PMO prior to reaction shows that Cu and especially Ni are uniformly dispersed on the catalyst (Figure 6a). After 168 h of reaction, Cu tends to aggregate into larger nanoparticles (up to 8 nm), while Ni still preserves a good dispersion, although with some agglomeration (Figure 6b). The EDS mapping results do not indicate the formation of MgO and Al_2O_3 aggregates during the reaction, as Mg and Al maintain good dispersion (Figure S12). A high-resolution TEM (HRTEM) image of CuNi-PMO after reaction (Figure S13) shows the presence of discrete metal particles. The lattice fringe (0.209 nm) corresponds to the (1 1 1) plane of a Cu phase (JCPDS card No. 00-004-0836).
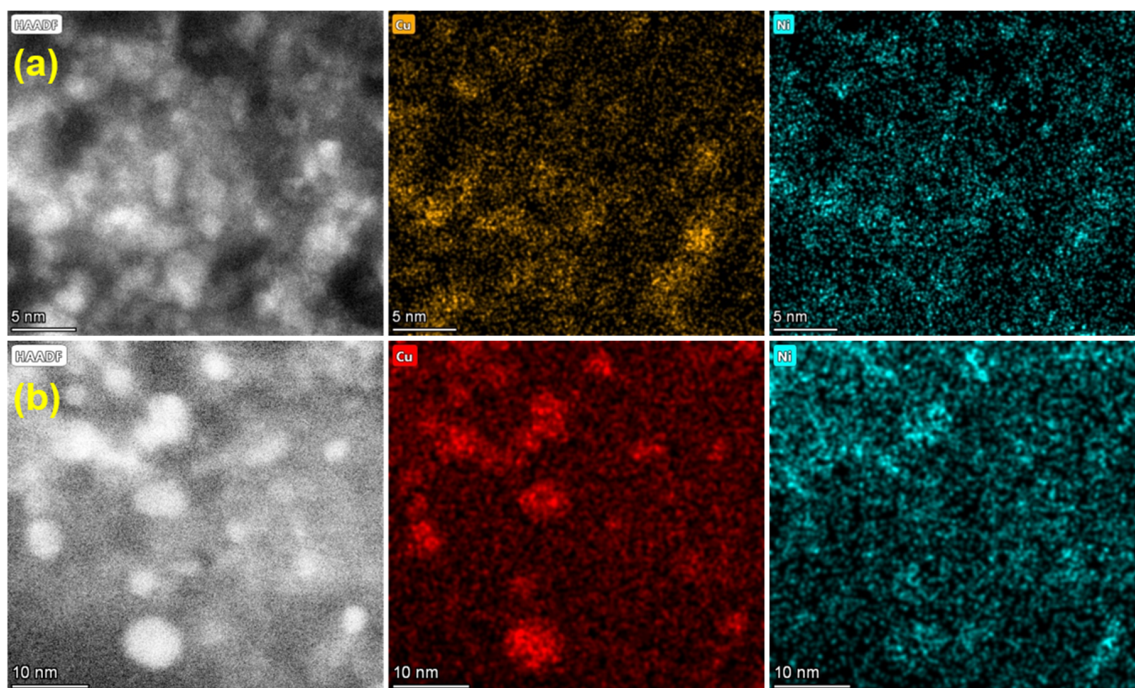
Figure 6. Dark-field TEM images and corresponding EDS mapping of Cu (red) and Ni (celeste) for fresh CuNi-PMO (**a**) and spent CuNi-PMO (**b**) obtained after 168 h.

These results indicate that the nanoparticles are Cu rich, and there is a close contact between these nanoparticles and the uniformly dispersed Ni species on the CuNi-PMO catalyst. The strong interaction between the Cu rich nanoparticles and Ni species (NiO) may reduce the tendency for agglomeration of the nanoparticles and have a positive effect on the stability of the CuNi-PMO catalyst [52].

In comparison, the average nanoparticle size (5.3 ± 1.0 nm, Figure S14a) for the monometallic Cu-PMO catalyst after reaction is a slightly larger than that for the bi-metallic CuNi-PMO, indicating a stabilizing effect of Ni regarding agglomeration. Nanoparticles were not observed for the spent Ni-PMO catalyst (Figure S14b), indicating that the NiO in this sample is difficult to reduce during the reaction, in line with H_2-TPR profiles (Figure S9).

The spent PMO catalysts were studied by TG analysis (Figure S15) to determine the amount and type of coke on the catalyst. The DTG profiles (Figure S16) for the three catalysts each show three mean peaks, but the intensity and exact position differs for the three spent catalysts. The small weight loss peak in the DTG below 200 °C is associated with the removal of adsorbed water and possibly some small organics. A considerable weight loss in the temperature range of 230–500 °C was observed, which is likely due to the presence of coke on the catalysts. Highest weight losses were found for Cu-PMO (23%), intermediate values for Ni-PMO (7.7%), and lowest for the bi-metallic one (6.3%). The DTG curve of Cu-PMO shows a large peak centered at 278 °C, indicating the presence of a soft coke [53–55]. The relatively high amounts of coke deposition on the Cu-PMO compared to bi-metallic CuNi-PMO catalyst is a possible reason for the lower carbon balance closures (Figure S4) and the decrease in activity of this catalyst in regime 2 (Figure 3).

Finally, the elemental composition of the CuNi-PMO catalysts after reaction (168 h) was determined using ICP-OES (Table S2). It clearly showed no major changes in the elemental composition before and after reaction, indicating that preferential leaching of one of the catalyst components is not occurring to a significant extent.

With the spent catalyst characterization data available, the changes in catalyst structure and morphology during reaction for the most relevant catalyst (bi-metallic Cu-Ni PMO) can be explained (Figure 7). Before reaction, the double-layered hydrotalcite precursors were calcined at 460 °C overnight, during which the lamellar structure is converted into an amorphous mixed-oxide with both CuO and

NiO homogeneously dispersed in the Mg-Al mixed oxide structure (Figures S1 and S2). In addition, H_2-TPR indicates that part of the CuO is dispersed on the catalyst surface (Figure 1). In the initial stage of the reaction, Cu^0 rich nanoparticles and likely also some Ni ones are formed by reaction with ethanol (TEM, Figure S8). Close contact between these nanoparticles and the uniformly dispersed NiO species (Figure 6) on the CuNi-PMO catalyst was observed as well. Most of the Ni though is present as Ni^{2+} (NiO, H_2-TPR). At longer runtimes, the size of the Cu nanoparticles (with possibly some Ni) increases slightly from 3 to 5 nm (TEM, Figure 5). This limited growth in nanoparticle size during runtimes is likely the reason for the good stability of the catalyst in regime 2, as observed experimentally.
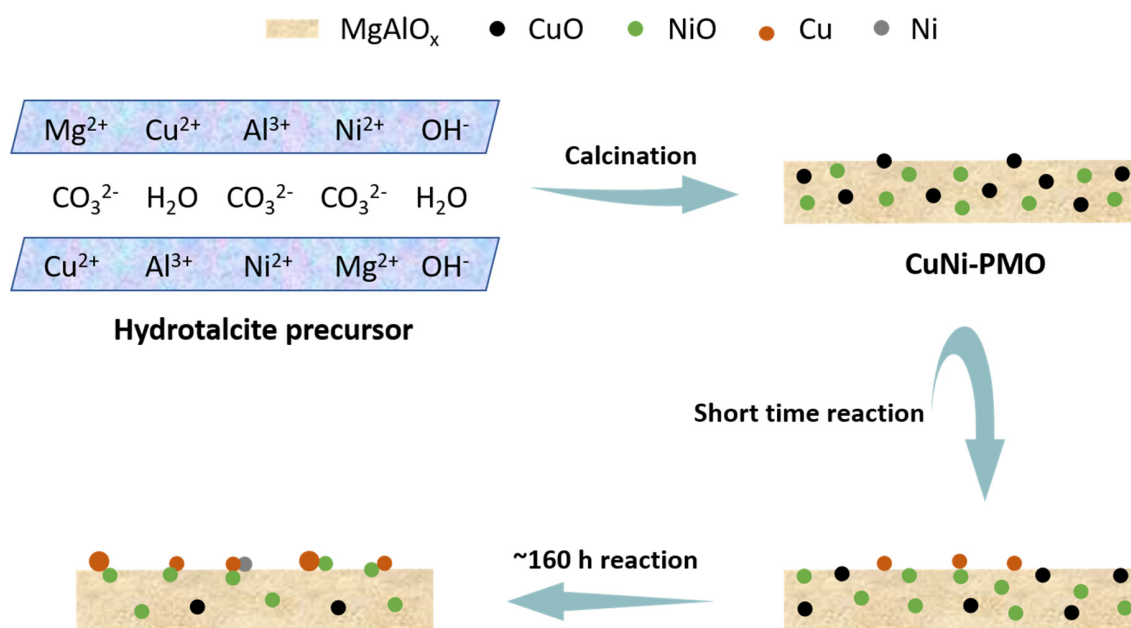

Figure 7. Schematic illustration of the formation of CuNi-PMO and its structural changes during reaction.

Finally, it is clear that the basicity increases in the initial stage of the reaction (regime 1) and then stays about constant in regime 2. Such an increase in basicity has also been reported in the literature [25] and ascribed to a (partial) structural transformation from the mixed oxides to the original hydrotalcite structure (memory effect) due to the formation of water during reaction (1 mol for the conversion of 2 moles of ethanol to one mole of 1-butanol, as well as water formation due to etherification) [56,57]. However, XRD analyses of spent catalysts do not show the presence of hydrotalcite peaks, thus this explanations likely does not hold here. An alternative explanation is the formation of basic metal-alkoxide species on the surface, as postulated by Carlini et al. in the Guerbet condensation of methanol with n-propanol [58].

Thus, the main changes in catalyst structure when going from regime 1 to regime 2 is a considerable increase in basicity and a limited growth in nanoparticle size of mainly Cu containing nanoparticles. As such, we ascribe the change in basicity as the major factor for the observed changes in conversion and chemoselectivity when going from regime 1 to 2. This is also in line with the basicity trend versus runtime, which shows major changes in regime 1 and stays about constant in regime 2. It is interesting to note that the log of the selectivity of 1-butanol increases linearly with the basicity of the catalysts (Figure S17).

In the very early stage of the reaction (initial stage of regime 1), the main product is acetaldehyde. As such, it appears that dehydrogenation of ethanol occurs to a significant extent by action of reduced Cu nanoparticles. Apparently, aldol condensation hardly occurs, likely because of the relatively low basicity of the support (Figure 4). At longer runtimes in regime 1, the ethanol conversion drops, and the chemoselectivity changes from acetaldehyde to 1-butanol. This change in chemoselectivity is in line with the observed increase in basicity of the support, facilitating the aldol condensation of

acetaldehyde and the subsequent dehydration/hydrogenation to 1-butanol. The reduction in ethanol conversion may be due to the strong adsorption of products (acetaldehyde and other (oligomeric) oxygenates). FTIR studies in the literature indeed support this hypothesis and show that oligomeric forms of formaldehyde and acetaldehyde block active sites and lead to reductions in catalyst activity.

After a certain period of time, ethanol conversion remains about constant (regime 2) and the product selectivity also does not change dramatically. Apparently, a stable catalyst is formed, supported by the spent catalyst characterization studies which show that the basicity is about constant and the average nanoparticle size only slightly increases. In addition, the amount of coke on the catalyst is relatively limited (6.3%).

2.4. Effects of Reaction Conditions and Reactor Configuration

A number of experiments (Figure S18) were performed at different temperatures (300, 360 °C) under atmospheric pressure and the result (Table 1) shows that the change in activity and selectivity versus run time is a generic feature of the catalyst under study. Higher temperature leads to a reduction in the runtime at which the change from regime 1 to regime 2 occurs. For example, the change from regime 1 to 2 was 144 h at 300 °C, and only 24 h at 360 °C. The highest 1-butanol selectivity in regime 2 was obtained at 320 °C due to relatively lower rates of consecutive reactions of 1-butanol to longer alcohols (2-ethyl-butanol (1%) and 1-hexanol (3%)) which are more pronounced at 360 °C.

Table 1. Ethanol conversion versus runtime and runtime to reach regime 2 at different temperatures over CuNi-PMO catalyst. Reaction conditions: 0.1 MPa, LHSV = 15 mL g^{-1} h^{-1}.

Temperature (°C)	Initial Ethanol Conversion (%)	Ethanol Conversion (%) in Regime 2	1-Butanol Selectivity (%) in Regime 2	Run Time (h) to Reach Regime 2
300	85.0	3.0	59.0	144
320	91.8	14.6	71.4	60
360	68.0	26.2	57.6	24

The effect of pressure was investigated by performing experiments at higher pressure (3, 7 MPa) and 320 °C (Figure S19). In this case, the runtime to reach regime 2 (stable ethanol conversion) was very low (<12 h), indicating a strong pressure effect on catalyst performance. Possible explanations for these temperature and pressure effects are likely related to the rate of changes in catalyst structure during the runs. For example, the rate of reduction of copper oxide and the formation of stabilized nanoparticles will be different at different conditions. In addition, at higher pressures, a shift from a gas phase to a supercritical phase may occur, which likely affects the relative mass transfer rates. Thus, a very beneficial effect of high pressure on ethanol conversion and 1-butanol yield was observed. Ethanol conversion of 47.3% and 62.5% 1-butanol selectivity was obtained at 7 MPa and 320 °C with a very promising space time yield of 1-butanol of 1.43 g_{pro} g_{cat}^{-1} h^{-1}.

The intriguing question arises what causes the major difference in catalyst performance between the continuous runs and earlier batch experiments (Table 2) performed in our group [28]. In the batch experiments, ethanol conversion increased with reaction time and the yield of 1-butanol was 21% after 6 h at 320 °C. Possible explanations for these differences are the accumulation of water in the batch reactor due to the occurrence of reactions leading to water formation (Scheme 1) and the presence of higher (autogenic) pressures in the batch experiments (typically 8 MPa at 320 °C). The accumulation of co-produced water in the batch reactor may have a profound and rapid effect on the basicity of the catalyst, and as a consequence change the chemoselectivity of the reaction already at much shorter times [56]. Pressure effects certainly play a role, as was seen for the continuous runs at various pressures at 320 °C, with high pressures leading to a fast change from regime 1 to regime 2.

Table 2. Ethanol conversion and 1-butanol yield with reaction time in a batch setup [1].

Reaction Time (h)	Ethanol Conversion (%)	1-Butanol Yield (%)
2	39.5	16.4
6	47.9	21.1
10	63.4	20.8
18	69.4	20.9

[1] Reaction conditions: CuNi-PMO (100 mg), ethanol (3 mL), 320 °C, 8 MPa (autogenic), decane (20 μL).

3. Experimental

3.1. Catalyst Preparation

The hydrotalcite catalyst precursors were prepared by a co-precipitation method, according to reported procedures [28]. Typically, a solution containing $MgCl_2 \cdot 6H_2O$ (0.06 mol, 12.2 g, ≥99.0%), $AlCl_3 \cdot 6H_2O$ (0.025 mol, 6.0 g, 99%), $Cu(NO_3)_2 \cdot 2.5H_2O$ (0.0075 mol, 1.74 g, 98%) and $Ni(NO_3)_2 \cdot 6H_2O$ (0.0075 mol, 2.18 g, ≥98.5% (KT)) in deionized water (0.1 L) was slowly added to an aqueous solution of Na_2CO_3 (0.025 mol, 1.0 g, ≥99.0%) at 60 °C under vigorous stirring for 72 h. The pH of the mixed solution was carefully maintained between 9 and 10 by addition of a solution of NaOH (1 M). After cooling to room temperature, the suspension was filtered. The solid was washed with deionized water and resuspended into an aqueous solution of Na_2CO_3 (2 M) at 40 °C under stirring for 24 h. The catalyst precursor was then filtered and washed with deionized water. The solid was dried at 120 °C overnight and the hydrotalcite precursor was obtained as blue powder. The corresponding CuNi-PMO was obtained after calcining the hydrotalcite material at 460 °C for 24 h in air. The monometallic Cu-PMO and Ni-PMO catalyst were prepared with the same procedure, replacing a defined amount of Mg^{2+} with Cu^{2+} and Ni^{2+}, respectively, while the M^{2+}/M^{3+} ratio was kept at a constant 3:1. The theoretical composition of the PMO catalysts is $Cu_{0.6}Mg_{2.4}Al_{1.0}$ (for Cu-PMO), $Ni_{0.6}Mg_{2.4}Al_{1.0}$ (for Ni-PMO), and $Cu_{0.3}Ni_{0.3}Mg_{2.4}Al_{1.0}$ (for CuNi-PMO). All the chemicals were purchased from Sigma-Aldrich Chemie GmbH, Schnelldorf, Germany.

3.2. Catalyst Characterization

The fresh and spent catalysts were characterized with ICP-OES (SPECTROBLUE) to quantify the elemental composition.

X-ray diffraction (XRD) spectra of the samples were collected in a 2θ scan range of 15–80° on a D8 Advance powder diffractometer (Bruker) with CuKα radiation (λ = 1.5418 Å) operated at 40 kV and 40 mA.

H_2-TPR measurements were conducted using 10 vol.% H_2 in He (30 mL min^{-1}) and the samples were heated from room temperature to 900 °C at a temperature ramp of 10 °C/min using an AutoChem system (Micromeritics) equipped with a thermal conductivity detector (TCD).

The basicity of the samples was determined by adsorption experiments with acrylic acid. The catalyst (20–40 mg) was suspended in a solution of acrylic acid in water (20–40 mL, ca. 10 mM) and stirred for 1 h in a closed vessel. The remaining concentration of acrylic acid was determined by HPLC (Agilent Technologies 1200 series, Waldbronn, Germany), equipped with a Bio-Rad Aminex HPX-87H column.

Attenuated total reflection-Fourier transform infrared (ATR-FTIR) spectra were collected in the wave number range of 400–4000 cm^{-1} with a resolution of 4 cm^{-1} on a VERTEX 70 spectrometer (Bruker, Leiderdorp, the Netherlands) equipped with an ATR geometry.

Transmission electron microscopy (TEM) measurements in a bright field mode were performed with a CM12 microscope (Philips) operating at 120 kV and a high-resolution microscope (JEOL 2010 FEG, Jena, Germany) operating at 200 kV. The samples were first ultrasonically dispersed in isopropanol and then deposited on holy carbon grids (400 mesh), which was subsequently dried with an IR lamp. High-angle annular dark-field scanning transmission electron microscopy (HAADF-STEM) images

were obtained with a ThemisZ microscope (Thermo Fischer Scientific, Tokyo, Japan) operating at 300 kV in STEM mode with a HAADF detector. Energy dispersive X-ray spectroscopy (EDS mapping) results were achieved with a Dual X EDS system (Bruker, Leiderdorp, The Netherlands). Data acquisition and analysis were done using Velox software (version 2.8.0).

Thermogravimetric analysis (TGA) was conducted on TGA/SDTA851e Analyzer (Mettler-Toledo). The samples were heated in a ceramic crucible from 50 to 900 °C at the heating rate of 10 °C min^{-1} under a flow of air (50 mL min^{-1}).

3.3. Catalytic Reactions

The catalysts were tested in a continuous reactor setup (Figure S20) equipped with a feed pump, a stainless steel reactor with a length of 4 cm and an inner diameter of 5 mm, a back pressure regulator, a gas–liquid separator, and a sample robot. It is worth noting that during the reactions described in this work, the gas exit was not used (closed) and only liquid product was collected. Typically, the catalyst (0.1 g, 100−200 um) was placed in the reactor tube and held in place by a stainless steel filter. The reactor was placed in an oven maintain a constant reaction temperature. Liquid ethanol (1.5 mL/h, 100% (*v/v*), technical grade) was fed continuously by an HPLC pump (Series I, Scientific Systems) and preheated before entering the reactor. Typical reaction conditions were 320 °C, 0.1 MPa, and a LHSV of 15 mL g^{-1} h^{-1}. A reaction was started by feeding ethanol for 24 h at room temperature to saturate the catalyst surface. Then, temperature was increased to the pre-set value and liquid product samples were collected every 12 h and analyzed by GC-FID (Hewlett-Packard 6890, Burladingen, Germany), equipped with an HP-5 capillary column. External and internal mass transfer limitations were excluded according to the methods reported in references [59,60]. The ethanol conversion, product distribution and yield, and carbon balance were calculated using Equations (1)−(4). A number of duplicate experiments were performed (Table S3), showing good reproducibility (±5% relative).

$$\text{Conversion} = \frac{\text{moles of ethanol in feed} - \text{moles of unreacted ethanol}}{\text{moles of ethanol in feed}} \tag{1}$$

$$\text{Carbon selectivity of product } i = \frac{\text{moles of carbon in product } i}{\text{moles of carbon in all products}} \tag{2}$$

$$\text{Yield of product } i = \frac{\text{moles of carbon in product } i}{2 * \text{moles of ethanol in feed}} \tag{3}$$

$$\text{Carbon balance} = \frac{\text{moles of carbon in all products and unreacted ethanol}}{\text{moles of carbon in feed ethanol}} \tag{4}$$

4. Conclusions

Hydrotalcite-derived mono- and bi-metallic CuNi-PMO catalysts were explored for the Guerbet coupling of ethanol to 1-butanol in a continuous flow setup with times on stream up to 160 h. Catalyst performance was best for the bi-metallic catalyst giving an ethanol conversion of 47.3% and a very promising space time yield of 1-butanol of 1.43 g$_{pro}$ g$_{cat}$$^{-1}$ h^{-1} (320 °C, 7 MPa, LHSV = 15 mL g^{-1} h^{-1}). When using the monometallic Ni-PMO catalyst, acetaldehyde was the main product, though only in limited amounts.

Two regimes with different product distributions were observed for Cu-PMO and CuNi-PMO catalyst with time on stream, with acetaldehyde in the first regime, and 1-butanol as the main product in the second one. Experiments at different temperatures and pressures show that the transition from regime 1 to 2 occurs at shorter runtimes when using higher temperatures and pressures.

Detailed characterization studies on spent CuNi-PMO catalysts at specific runtimes revealed that the change in chemoselectivity from acetaldehyde to 1-butanol with runtime is mainly due to an

increase of the basicity of the catalyst and neither to major changes in the type and size of metallic nanoparticles, nor to major changes in morphology.

Distinct differences in catalyst performance in the continuous packed bed and batch reactor were observed, and this effect was strongest when working at lower pressure in the continuous setup. This is likely due to accumulation of water and the use of higher (autogenous) pressures in batch systems. As such, batch experiments, even when using multiple reaction–catalyst recycles, are not providing conclusive information on the extent of catalyst deactivation, highly relevant information for scale-up of the chemistry. For this purpose, dedicated experimentation in continuous setups is required.

Supplementary Materials: The following are available online at http://www.mdpi.com/2073-4344/10/9/996/s1.

Conflicts of Interest: The authors declare no conflict of interest.

References

1. Ragauskas, A.J.; Williams, C.K.; Davison, B.H.; Britovsek, G.; Cairney, J.; Eckert, C.A.; Frederick, W.J.; Hallett, J.P.; Leak, D.J.; Liotta, C.L.; et al. The Path Forward for Biofuels and Biomaterials. *Science* **2006**, *311*, 484. [CrossRef] [PubMed]

2. Eagan, N.M.; Kumbhalkar, M.D.; Buchanan, J.S.; Dumesic, J.A.; Huber, G.W. Chemistries and processes for the conversion of ethanol into middle-distillate fuels. *Nat. Rev. Chem.* **2019**, *3*, 223–249. [CrossRef]

3. Balat, M. Production of bioethanol from lignocellulosic materials via the biochemical pathway: A review. *Energy Convers. Manag.* **2011**, *52*, 858–875. [CrossRef]

4. Sun, Y.; Cheng, J. Hydrolysis of lignocellulosic materials for ethanol production: A review. *Bioresour. Technol.* **2002**, *83*, 1–11. [CrossRef]

5. Trindade, W.R.D.S.; Santos, R.G.D. Review on the characteristics of butanol, its production and use as fuel in internal combustion engines. *Renew. Sustain. Energy Rev.* **2017**, *69*, 642–651. [CrossRef]

6. Devarapalli, M.; Atiyeh, H.K. A review of conversion processes for bioethanol production with a focus on syngas fermentation. *Biofuel Res. J.* **2015**, *2*, 268–280. [CrossRef]

7. Luk, H.T.; Mondelli, C.; Ferré, D.C.; Stewart, J.A.; Pérez-Ramírez, J. Status and prospects in higher alcohols synthesis from syngas. *Chem. Soc. Rev.* **2017**, *46*, 1358–1426. [CrossRef]

8. Gabriëls, D.; Hernández, W.Y.; Sels, B.; Van Der Voort, P.; Verberckmoes, A. Review of catalytic systems and thermodynamics for the Guerbet condensation reaction and challenges for biomass valorization. *Catal. Sci. Technol.* **2015**, *5*, 3876–3902. [CrossRef]

9. Sun, Z.; Barta, K. Cleave and couple: Toward fully sustainable catalytic conversion of lignocellulose to value added building blocks and fuels. *Chem. Commun.* **2018**, *54*, 7725–7745. [CrossRef]

10. Hanspal, S.; Young, Z.D.; Prillaman, J.T.; Davis, R.J. Influence of surface acid and base sites on the Guerbet coupling of ethanol to butanol over metal phosphate catalysts. *J. Catal.* **2017**, *352*, 182–190. [CrossRef]

11. Marcu, I.-C.; Tanchoux, N.; Fajula, F.; Tichit, D. Catalytic conversion of ethanol into butanol over M–Mg–Al mixed oxide catalysts (M= Pd, Ag, Mn, Fe, Cu, Sm, Yb) obtained from LDH precursors. *Catal. Lett.* **2013**, *143*, 23–30. [CrossRef]

12. León, M.; Díaz, E.; Vega, A.; Ordóñez, S.; Auroux, A. Consequences of the iron–aluminium exchange on the performance of hydrotalcite-derived mixed oxides for ethanol condensation. *Appl. Catal. B Environ.* **2011**, *102*, 590–599. [CrossRef]

13. Chieregato, A.; Velasquez, O.J.; Bandinelli, C.; Fornasari, G.; Cavani, F.; Mella, M. On the Chemistry of Ethanol on Basic Oxides: Revising Mechanisms and Intermediates in the Lebedev and Guerbet reactions. *Chem. Sustain. Chem.* **2015**, *8*, 377–388. [CrossRef] [PubMed]

14. Kozlowski, J.T.; Davis, R.J. Heterogeneous catalysts for the Guerbet coupling of alcohols. *ACS Catal.* **2013**, *3*, 1588–1600. [CrossRef]

15. Wu, X.; Fang, G.; Tong, Y.; Jiang, D.; Liang, Z.; Leng, W.; Liu, L.; Tu, P.; Wang, H.; Ni, J. Catalytic Upgrading of Ethanol to n-Butanol: Progress in Catalyst Development. *Chem. Sustain. Chem.* **2018**, *11*, 71–85. [CrossRef] [PubMed]

16. Di Cosimo, J.I.; Apesteguı, A.C.R.; Ginés, M.J.L.; Iglesia, E. Structural requirements and reaction pathways in condensation reactions of alcohols on MgyAlOx catalysts. *J. Catal.* **2000**, *190*, 261–275. [CrossRef]

17. Moteki, T.; Flaherty, D.W. Mechanistic insight to C–C bond formation and predictive models for cascade reactions among alcohols on Ca-and Sr-hydroxyapatites. *ACS Catal.* **2016**, *6*, 4170–4183. [CrossRef]

18. Ho, C.R.; Shylesh, S.; Bell, A.T. Mechanism and kinetics of ethanol coupling to butanol over hydroxyapatite. *ACS Catal.* **2016**, *6*, 939–948. [CrossRef]

19. Nishimura, S.; Takagaki, A.; Ebitani, K. Characterization, synthesis and catalysis of hydrotalcite-related materials for highly efficient materials transformations. *Green Chem.* **2013**, *15*, 2026–2042. [CrossRef]

20. Di Cosimo, J.I.; Dıez, V.K.; Xu, M.; Iglesia, E.; Apesteguıa, C.R. Structure and surface and catalytic properties of Mg-Al basic oxides. *J. Catal.* **1998**, *178*, 499–510. [CrossRef]

21. Cavani, F.; Trifiro, F.; Vaccari, A. Hydrotalcite-type anionic clays: Preparation, properties and applications. *Catal. Today* **1991**, *11*, 173–301. [CrossRef]

22. Zaccheria, F.; Scotti, N.; Ravasio, N. The Role of Copper in the Upgrading of Bioalcohols. *Chem. Cat. Chem.* **2018**, *10*, 1526–1535. [CrossRef]

23. Bravo-Suárez, J.J.; Subramaniam, B.; Chaudhari, R.V. Vapor-phase methanol and ethanol coupling reactions on CuMgAl mixed metal oxides. *Appl. Catal. A Gen.* **2013**, *455*, 234–246. [CrossRef]

24. Cheng, F.; Guo, H.; Cui, J.; Hou, B.; Xi, H.; Jia, L.; Li, D. Coupling of methanol and ethanol over CuMgAlOx catalysts: The roles of copper species and alkalinity. *React. Kinet. Mech. Catal.* **2019**, *126*, 119–136. [CrossRef]

25. Benito, P.; Vaccari, A.; Antonetti, C.; Licursi, D.; Schiarioli, N.; Rodriguez-Castellón, E.; Raspolli Galletti, A.M. Tunable copper-hydrotalcite derived mixed oxides for sustainable ethanol condensation to n-butanol in liquid phase. *J. Clean. Prod.* **2019**, *209*, 1614–1623. [CrossRef]

26. Alonso, D.M.; Wettstein, S.G.; Dumesic, J.A. Bimetallic catalysts for upgrading of biomass to fuels and chemicals. *Chem. Soc. Rev.* **2012**, *41*, 8075–8098. [CrossRef]

27. Hernández, W.Y.; De Vlieger, K.; Van Der Voort, P.; Verberckmoes, A. Ni–Cu Hydrotalcite-Derived Mixed Oxides as Highly Selective and Stable Catalysts for the Synthesis of β-Branched Bioalcohols by the Guerbet Reaction. *Chem. Sustain. Chem.* **2016**, *9*, 3196–3205. [CrossRef]

28. Sun, Z.; Couto Vasconcelos, A.; Bottari, G.; Stuart, M.C.A.; Bonura, G.; Cannilla, C.; Frusteri, F.; Barta, K. Efficient Catalytic Conversion of Ethanol to 1-Butanol via the Guerbet Reaction over Copper- and Nickel-Doped Porous. *ACS Sustain. Chem. Eng.* **2017**, *5*, 1738–1746. [CrossRef]

29. Jordison, T.L.; Peereboom, L.; Miller, D.J. Impact of water on condensed phase ethanol Guerbet reactions. *Ind. Eng. Chem. Res.* **2016**, *55*, 6579–6585. [CrossRef]

30. Quesada, J.; Faba, L.; Díaz, E.; Ordóñez, S. Role of the surface intermediates in the stability of basic mixed oxides as catalyst for ethanol condensation. *Appl. Catal. A Gen.* **2017**, *542*, 271–281. [CrossRef]

31. Silvester, L.; Lamonier, J.-F.; Faye, J.; Capron, M.; Vannier, R.-N.; Lamonier, C.; Dubois, J.L.; Couturier, J.L.; Calais, C.; Dumeignil, F. Reactivity of ethanol over hydroxyapatite-based Ca-enriched catalysts with various carbonate contents. *Catal. Sci. Technol.* **2015**, *5*, 2994–3006. [CrossRef]

32. Kannan, S.; Dubey, A.; Knozinger, H. Synthesis and characterization of CuMgAl ternary hydrotalcites as catalysts for the hydroxylation of phenol. *J. Catal.* **2005**, *231*, 381–392. [CrossRef]

33. Takehira, K.; Shishido, T.; Wang, P.; Kosaka, T.; Takaki, K. Autothermal reforming of CH4 over supported Ni catalysts prepared from Mg–Al hydrotalcite-like anionic clay. *J. Catal.* **2004**, *221*, 43–54. [CrossRef]

34. Tuza, P.V.; Manfro, R.L.; Ribeiro, N.F.P.; Souza, M.M.V.M. Production of renewable hydrogen by aqueous-phase reforming of glycerol over Ni–Cu catalysts derived from hydrotalcite precursors. *Renew. Energy* **2013**, *50*, 408–414. [CrossRef]

35. Tanasoi, S.; Tanchoux, N.; Urdă, A.; Tichit, D.; Săndulescu, I.; Fajula, F.; Marcu, I.C. New Cu-based mixed oxides obtained from LDH precursors, catalysts for methane total oxidation. *Appl. Catal. A Gen.* **2009**, *363*, 135–142. [CrossRef]

36. Han, J.; Zeng, H.Y.; Xu, S.; Chen, C.R.; Liu, X.J. Catalytic properties of CuMgAlO catalyst and degradation mechanism in CWPO of methyl orange. *Appl. Catal. A Gen.* **2016**, *527*, 72–80. [CrossRef]

37. Yu, X.-P.; Chu, W.; Wang, N.; Ma, F. Hydrogen Production by Ethanol Steam Reforming on NiCuMgAl Catalysts Derived from Hydrotalcite-Like Precursors. *Catal. Lett.* **2011**, *141*, 1228–1236. [CrossRef]

38. Li, Q.; Yi, H.; Tang, X.; Zhao, S.; Zhao, B.; Liu, D.; Gao, F. Preparation and characterization of Cu/Ni/Fe hydrotalcite-derived compounds as catalysts for the hydrolysis of carbon disulfide. *Chem. Eng. J.* **2016**, *284*, 103–111. [CrossRef]

39. Li, D.; Koike, M.; Chen, J.; Nakagawa, Y.; Tomishige, K. Preparation of Ni–Cu/Mg/Al catalysts from hydrotalcite-like compounds for hydrogen production by steam reforming of biomass tar. *Int. J. Hydrogen Energy* **2014**, *39*, 10959–10970. [CrossRef]

40. Montanari, B.; Vaccari, A.; Gazzano, M.; Käßner, P.; Papp, H.; Pasel, J.; Dziembaj, R.; Makowski, W.; Lojewski, T. Characterization and activity of novel copper-containing catalysts for selective catalytic reduction of NO with NH3. *Appl. Catal. B Environ.* **1997**, *13*, 205–217. [CrossRef]

41. Ashok, J.; Subrahmanyam, M.; Venugopal, A. Hydrotalcite structure derived Ni–Cu–Al catalysts for the production of H2 by CH4 decomposition. *Int. J. Hydrogen Energy* **2008**, *33*, 2704–2713. [CrossRef]

42. Chmielarz, L.; Kuśtrowski, P.; Rafalska-Łasocha, A.; Dziembaj, R. Selective oxidation of ammonia to nitrogen on transition metal containing mixed metal oxides. *Appl. Catal. B Environ.* **2005**, *58*, 235–244. [CrossRef]

43. Dragoi, B.; Ungureanu, A.; Chirieac, A.; Ciotonea, C.; Rudolf, C.; Royer, S.; Dumitriu, E. Structural and catalytic properties of mono-and bimetallic nickel–copper nanoparticles derived from MgNi (Cu) Al-LDHs under reductive conditions. *Appl. Catal. A Gen.* **2015**, *504*, 92–102. [CrossRef]

44. Parida, K.; Das, J. Mg/Al hydrotalcites: Preparation, characterisation and ketonisation of acetic acid. *J. Mol. Catal. A Chem.* **2000**, *151*, 185–192. [CrossRef]

45. Delidovich, I.; Palkovits, R. Structure–performance correlations of Mg–Al hydrotalcite catalysts for the isomerization of glucose into fructose. *J. Catal.* **2015**, *327*, 1–9. [CrossRef]

46. Abelló, S.; Medina, F.; Tichit, D.; Pérez-Ramírez, J.; Groen, J.C.; Sueiras, J.E.; Salagre, P.; Cesteros, Y. Aldol condensations over reconstructed Mg–Al hydrotalcites: Structure–activity relationships related to the rehydration method. *Chem. A Eur. J.* **2005**, *11*, 728–739. [CrossRef]

47. Lee, G.; Jeong, Y.; Takagaki, A.; Jung, J.C. Sonication assisted rehydration of hydrotalcite catalyst for isomerization of glucose to fructose. *J. Mol. Catal. A Chem.* **2014**, *393*, 289–295. [CrossRef]

48. Satta, A.; Shamiryan, D.; Baklanov, M.R.; Whelan, C.M.; Le, Q.T.; Beyer, G.P.; Vantomme, A.; Maex, K. The removal of copper oxides by ethyl alcohol monitored in situ by spectroscopic ellipsometry. *J. Electrochem. Soc.* **2003**, *150*, G300–G306. [CrossRef]

49. Coskun, F.; Cetinkaya, S.; Eroglu, S. Reduction of Nickel Oxide with Ethanol. *JOM* **2017**, *69*, 987–992. [CrossRef]

50. Macala, G.S.; Matson, T.D.; Johnson, C.L.; Lewis, R.S.; Iretskii, A.V.; Ford, P.C. Hydrogen transfer from supercritical methanol over a solid base catalyst: A model for lignin depolymerization. *Chem. Sustain. Energy Mater.* **2009**, *2*, 215–217. [CrossRef]

51. Kumar, A.; Cross, A.; Manukyan, K.; Bhosale, R.R.; van den Broeke, L.J.P.; Miller, J.T.; Mukasyan, A.S.; Wolf, E.E. Combustion synthesis of copper–nickel catalysts for hydrogen production from ethanol. *Chem. Eng. J.* **2015**, *278*, 46–54. [CrossRef]

52. Jiang, D.; Wu, X.; Mao, J.; Ni, J.; Li, X. Continuous catalytic upgrading of ethanol to n-butanol over Cu–CeO 2/AC catalysts. *Chem. Commun.* **2016**, *52*, 13749–13752. [CrossRef] [PubMed]

53. Ahmed, R.; Sinnathambi, C.M.; Subbarao, D. Kinetics of de-coking of spent reforming catalyst. *J. Appl. Sci.* **2011**, *11*, 1225–1230. [CrossRef]

54. Behera, B.; Ray, S.S. Structural changes of FCC catalyst from fresh to regeneration stages and associated coke in a FCC refining unit: A multinuclear solid state NMR approach. *Catal. Today* **2009**, *141*, 195–204. [CrossRef]

55. Kosinov, N.; Uslamin, E.A.; Coumans, F.J.A.G.; Wijpkema, A.S.G.; Rohling, R.Y.; Hensen, E.J.M. Structure and evolution of confined carbon species during methane dehydroaromatization over Mo/ZSM-5. *ACS Catal.* **2018**, *8*, 8459–8467. [CrossRef]

56. Prinetto, F.; Ghiotti, G.; Durand, R.; Tichit, D. Investigation of Acid−Base Properties of Catalysts Obtained from Layered Double Hydroxides. *J. Phys. Chem. B* **2000**, *104*, 11117–11126. [CrossRef]

57. Marcu, I.-C.; Tichit, D.; Fajula, F.; Tanchoux, N. Catalytic valorization of bioethanol over Cu-Mg-Al mixed oxide catalysts. *Catal. Today* **2009**, *147*, 231–238. [CrossRef]

58. Carlini, C.; Flego, C.; Marchionna, M.; Noviello, M.; Galletti, A.M.R.; Sbrana, G.; Basile, F.; Vaccari, A. Guerbet condensation of methanol with n-propanol to isobutyl alcohol over heterogeneous copper chromite/Mg–Al mixed oxides catalysts. *J. Mol. Catal. A Chem.* **2004**, *220*, 215–220. [CrossRef]

59. Mears, D.E. Tests for transport limitations in experimental catalytic reactors. *Ind. Eng. Chem. Process. Des. Dev.* **1971**, *10*, 541–547. [CrossRef]

60. Weisz, P.B.; Prater, C.D. Interpretation of measurements in experimental catalysis. *Adv. Catal.* **1954**, *6*, 60390–60399.